Investigation on Hovering Rotors over Inclined Ground Planes – a Computational and Experimental Study

Stefan Platzer *

Institute of Helicopter Technology, Technical University of Munich, 80333 Munich, Germany

Joseph Milluzzo †

United States Naval Academy, Annapolis, MD 21402, USA

Jürgen Rauleder ‡

Institute of Helicopter Technology, Technical University of Munich, 80333 Munich, Germany

The influence of time-varying ground effect (e.g., induced by ship deck motion) or even of static, inclined ground planes (e.g., hillsides) on the flow field and on the rotor inflow in hover is not yet understood. Therefore, experiments and CFD simulations were performed to study the flow field below a two-bladed 0.8 m-diameter rotor in hover over a parallel and a 15 degree inclined ground plane at a height of one rotor radius above the ground plane pivot point. Particle image velocimetry measurements were used to measure the rotor wake, and CFD simulations were correlated to the experimental results. To investigate the flow field, instantaneous, phase-averaged, and time-averaged data were used. The flow field was found to be sensitive to the ground plane inclination angle. It was found that the inclined ground plane reduced the unsteadiness in the flow field. The phase-averaged experimental results were predicted well by the numerical simulation. The computations captured the flow phenomenology well, but underestimated the influence of the inclined ground plane on the rotor inflow.

NOMENCLATURE

A	Rotor disk area, $= \pi R^2$, m^2
c	Rotor blade chord length, m
l	Distance from vortex center, m
C_T	Rotor thrust coefficient, $= T/\rho A(\Omega R)^2$
M_{tip}	Mach number at blade tip
N	Number of points
N_b	Number of rotor blades
P	Point in data set
$\mathbf{P}$	Radius vector, m
r	Radial distance from rotational axis, m
R	Rotor radius, m
Re_{tip}	Chord Reynolds number at blade tip, $= V_{\text{tip}} c\rho/\mu$
S	Area
T	Rotor thrust, N
$\mathbf{U}$	Velocity vector, m s^{-1}
V_{farfield}	Velocity at farfield boundary, m s^{-1}
v_h	Hover induced velocity, $= \sqrt{T/(2\rho A)}$, m s^{-1}
V_{tip}	Rotor tip speed, $= \Omega R$, m s^{-1}
v_z	Vertical velocity component, m s^{-1}
y^+	Dimensionless wall distance
z	Height over ground, m
$\mathbf{z}$	Unit vector normal to plane
Γ_1	Non-dimensional scalar quantity
ζ	Wake age of the tip vortex, $= \Omega t$, deg.
Θ_0	Blade collective pitch angle, deg.
Θ_{GP}	Ground plane inclination angle, deg.
Θ_M	Angle between velocity vector and radius vector, deg.
μ	Dynamic viscosity, kg m^{-1} s^{-1}
$\tilde{\nu}$	Spalart–Allmaras viscosity
ρ	Air density, kg m^{-3}
σ	Standard deviation
ψ_b	Rotor blade azimuth angle, deg.
Ω	Angular velocity of the rotor, rad s^{-1}

* Graduate Research Assistant. stefan.platzer@tum.de

† Assistant Professor. milluzzo@usna.edu

‡ Lecturer. juergen.rauleder@tum.de

Presented at the 44th European Rotorcraft Forum, Delft, The Netherlands, Sept. 18-20, 2018.

1. INTRODUCTION

Rotorcraft regularly operate in complex flight conditions, such as hover over inclined ground surfaces (e.g., hill-

sides and mountains) or moving surfaces (e.g. ship decks). However, only little is known about the complex three-dimensional flow field in the rotor wake and the associated inflow distribution in the rotor plane in these flight conditions. Significant training as well as expensive flight tests are required to mitigate the risk in helicopter operations on ships or at hillsides/mountains, and advanced flight control systems are desirable to increase safety and reduce pilot workload.

Moreover, as the range of application of unmanned aerial systems is ever-increasing, engineers and researchers need to be able to accurately model such flight conditions when designing control systems for them. Therefore, there is a need for accurate, computationally efficient mathematical models capable of simulating the rotor inflow in these complex flow environments, because it changes the rotorcraft flight dynamics. Dynamic inflow-type models could fill this role. However, a prerequisite to developing such models is an understanding of the complex three-dimensional fluid dynamics of the problem, which does not exist to date.

Previous research activities on hover in ground effect mostly focused on parallel ground planes. The performance benefits [1–5] and flow topology associated with hover in ground effect over parallel ground planes are relatively well known [6–9]. However, only a very limited amount of work has been done on non-parallel ground planes and the associated changes of the flow field [10, 11]. Kocak used flow visualization and laser doppler anemometry (LDA) to examine a rotor hovering in ground effect above a 10° inclined ground plane [10]. This study documented a change in the mean induced velocity between the uphill and downhill sides of the rotor, but only the outboard region near the blade tip was examined. Furthermore, because of the qualitative nature of flow visualization, the wake could not be quantitatively defined. Newman [11] also investigated rotors operating near inclined and moving surfaces. However, the focus of the work was on the effects of horizontal gusts on blade sailing and blade flapping behavior, and it did not consider the effects of the ground on the rotor wake structure.

For numerical methods, such as CFD, hover-in-ground (IGE) effect simulations are very challenging and are associated with high computational cost. Especially the necessity to accurately convect and preserve the tip vortex to late wake ages, i.e., to transport the tip vortex downstream to the ground plane, increases mesh sizes and thus computing time substantially. Nevertheless, multiple researchers have numerically simulated rotors in ground effect; see e.g. [12–14]. While free vortex wake methods can reduce some of the computational cost associated with modeling rotor wakes in ground effect, they require empirical constants that must be obtained from experimentation or higher-fidelity methods [15, 16]. However, all of these works examined rotors operating above a stationary, parallel ground.

Over the past two decades, considerable work has been performed on the development of dynamic inflow state-space models capable of modeling static and dynamic ground effect [17, 18]. These models expanded on the Peters–He finite-state dynamic inflow model treating the influence of the ground plane on rotor inflow as a source-like pressure perturbation in the flow field [17]. These methods have been validated for static parallel ground effect conditions [18]. However, the lack of experimental data for inclined and dynamic ground effect conditions limited the ability for validation.

The objective of the present work was to investigate the fluid mechanics of a hovering rotor over non-parallel ground planes by means of finite-volume computational fluid dynamics and experiments. In particular, the effects of the non-parallel ground plane on the tip vortex locations, tip vortex strength, and inflow distributions were investigated in detail. Furthermore, the effect of averaging the data was examined and compared to the CFD results.

2. DESCRIPTION OF THE TEST CASE

A two-bladed teetering rotor of radius $R = 0.408$ m was investigated in hover in ground effect. The stiff, untwisted blades had a constant chord length ($c = 44.5$ mm) and constant airfoil section (NACA 0012). In the experiments, the collective blade pitch was set to $\Theta_0 = 6^\circ$ and two different ground plane inclination angles, namely $\Theta_{GP} = 0^\circ$ and $\Theta_{GP} = 15^\circ$, were examined. For the numerical simulations, the collective blade pitch angle was trimmed to closely approximate the respective thrust in the experiment, resulting in $\Theta_0 = 7.3^\circ$ for the parallel and $\Theta_0 = 7.1^\circ$ for the inclined ground plane. A rotational frequency of 35 Hz (2100 rpm) yielded a blade tip speed of 89.7 $\mathrm{m\,s^{-1}}$, a tip Mach number of $M_{tip} = 0.27$ and a chord Reynolds number of $Re_{tip} = 280,000$ at the blade tip. The rotor parameters are summarized in Table 1.

For all IGE test points, the rotor plane was located at a height of $z/R = 1.0$ above the ground plane pivot point; see Fig. 1. That is, the rotor head remained fixed relative to the pivot point. In the experiment, the rotor could freely respond to changing ground plane inclination angles by a flapping motion. However, the possible flapping response of the rotor due to a changed ground plane angle could not be measured experimentally using the current setup. In the simulations the rotor was clamped and a flapping motion was not simulated.

The ground plane had a diameter of four rotor radii. To limit flow recirculation within the facility flow diverters were mounted along the circumference of the ground plane; see Fig. 2. In the numerical simulations the same diameter was used for the ground plane. However, the flow diverters were not modeled.

3. DESCRIPTION OF THE EXPERIMENTS

Two test were conducted using the same experimental setup; see Fig. 1. The first one was used to create a database

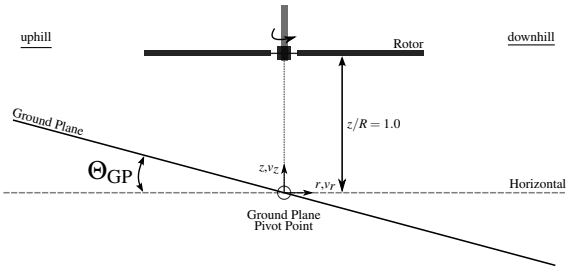

Fig. 1: Schematic showing the rotor-ground plane orientation at a rotor azimuth angle of $\psi_b = 0°$.

Table 1: Summary of rotor parameters.

Number of Blades, N_b	2
Blade Radius, R	0.408 m
Mean Chord, c	44.45 mm
Airfoil	NACA 0012
Rotational Frequency, Ω	35 Hz (2100 rpm)
Tip Speed, V_{tip}	89.7 m s^{-1}
Tip Mach Number, M_{tip}	0.27
Tip Reynolds Number, Re_{tip}	280,000

for analyzing the instantaneous and phase-averaged flow field at a rotor azimuth of $\psi_b = 0°$ using particle image velocimetry (PIV). A total of 500 instantaneous flow field realizations were taken for each of the two test cases (two Θ_{GP}) investigated in the present study.

A second test campaign was used to investigate the time-averaged inflow below the rotor for each of the two test cases (i.e., two Θ_{GP}) by averaging instantaneous flow field realizations. Equally spaced azimuthal increments ($\Delta\psi_b = 10°$) were used over the complete blade azimuth range (i.e., $0° \leq \psi_b < 360°$), to prevent biasing the average. The alignment between the ground plane, laser and cameras was not altered compared to the first test campaign; see Fig. 1. At each blade azimuth position, ten flow field realizations were recored, which resulted in a total of 360 instantaneous flow field realizations per test case (i.e., per investigated ground plane inclination angle).

3.1 Performance Measurements

A six-axis load cell was used to measure the rotor thrust produced and torque required as a function of the blade collective pitch. The contribution of the hub to the measured loads (determined by rotating the hub without the blades attached) was removed from the measurements. The results of the performance analysis were previously presented [19] for six different ground plane inclination angles ($\Theta_{GP} = 0°$ to $\Theta_{GP} = 30°$). In the present study, performance is not of particular interest and only relevant thrust values will be given.

Fig. 2: Photograph of the ground plane with flow diverters [19].

3.2 Flow Field Measurements

Flow field measurements were performed using phase-resolved two-component particle image velocimetry (PIV). The basic set up of the laser and cameras is shown in Fig. 3. The imaging axis of the cameras was aligned orthogonal to the plane of the light sheet. The light sheet was focused on the desired region of interest (ROI) shown in Fig. 4, and positioned along the trailing edge of the downhill facing blade; see Figs. 1 and 5. Hence, for the uphill blade the measurement was made in front of the leading edge, whereas for the downhill blade data was recorded behind the trailing edge. The ROI was chosen such that the rotor wake could be examined from the rotor plane downstream to the ground plane for both ground plane inclination angles. The cameras and the laser were digitally synchronized such that the laser pulses straddled the camera images.

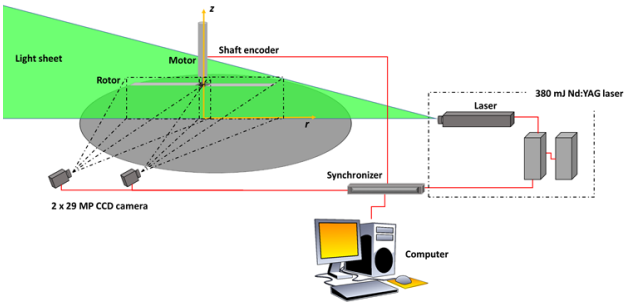

Fig. 3: Schematic showing the two-bladed rotor and the experimental setup with the laser and the cameras used for PIV.

The flow field measurements were performed using two 29 mega pixel CCD cameras (6600-by-4400 pixel) and a Nd:YAG laser capable of 380 mJ/pulse when operated at frequencies below 10 Hz. The imaging system and rotor rotational frequency were synchronized because the rotational frequency of the rotor (35 Hz) exceeded the maximum imaging rate of the cameras (1.8 Hz). The synchronization process resulted in PIV images being acquired at sub-integer multiples of the rotor frequency (i.e., one image approximately every 35 rotor revolutions).

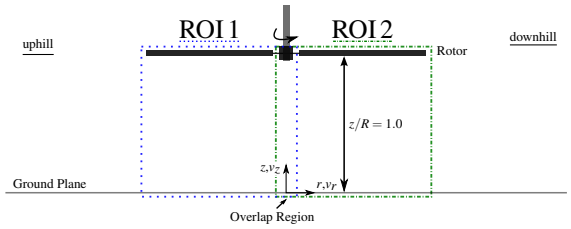

Fig. 4: Definition of the coordinate system and the regions of interest (ROI) used for flow field measurements.

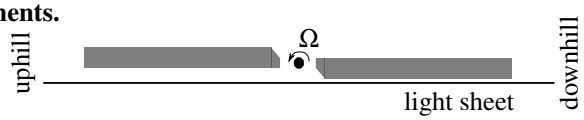

Fig. 5: Schematic showing a top view of the rotor assembly with the laser light sheet.

Multiple ROIs were required to provide the necessary spatial resolution and particle image size over the entire field of interest; see Fig. 4. Therefore, the cameras were positioned adjacent to each other with an overlap in their field of view. Mosaicing of the temporally correlated PIV images was used to increase the effective field of view without degrading the spatial resolution. The high resolution of the cameras allowed for a large ROI while maintaining the necessary measurement resolution. The measurements were performed with each camera focusing on an initial ROI of approximately 470 x 700 mm (1.15 x 1.72 R) with a 55 mm overlap in their fields of view, resulting in a total mosaiced field of view of 890 x 700 mm (2.18 x 1.72 R).

For all the flow field measurements, a recursive cross-correlation technique was used, which performed a final pass using an interrogation window size of 48-by-48 pixel and a 75% overlap. A local median filter was applied to the processed PIV data that removed vectors of more than twice the standard deviation of the median of the 3-by-3 neighboring vectors. Images containing more than 5% removed vectors were excluded from any further analysis.

4. DESCRIPTION OF THE NUMERICAL METHODOLOGY

For the present numerical study, the CFD solver TAU (release 2017.1.0) developed by the German Aerospace Center (DLR) was used [20]. This finite volume solver is capable of handling unstructured as well as structured grids and has a second-order accuracy in time and space. The rotor blades were assumed to be stiff, i.e., blade flapping, bending or teetering was not modeled.

4.1 Numerical Settings and Boundary Conditions

The viscous flow calculations were performed using the unsteady Reynolds-averaged Navier–Stokes (URANS) equations with the one-equation Spalart–Allmaras turbulence model, including a modification for negative values of the Spalart–Allmaras viscosity $\tilde{\nu}$ (SA-neg model). The turbulence model was used with rotation/curvature correction (sarc) to improve the vortex preservation. All simulations were run with a CFL-number of 8. To accelerate convergence of the solution, a two-stage multigrid cycle was used. For the time-accurate computations, dual time stepping was used with an implicit backward Euler scheme.

The viscous and convective fluxes were discretized using a second-order central scheme. At the cell faces, the convective mean flow flux was computed as *flux of average* and the convective turbulence flux as *Roe2nd*. Matrix dissipation was added to stabilize the solution using a second order dissipation coefficient of 0.1 and fourth order dissipation coefficient of 64. The matrix dissipation operator was applied to the mean flow equations and the turbulence equations.

The blade surface was modeled as a fully turbulent viscous wall, i.e., transition was not calculated or prescribed. For all simulations a wall spacing of $y+ < 1$ was achieved. Hence, the boundary layer was resolved and wall functions were not used. The ground plane was modeled as an impermeable frictionless surface. At the farfield boundaries, the initial velocity and all gradients were set to zero.

4.2 Meshing Strategy

In order to decrease numerical dissipation of the tip vortices, fully structured, cylindrical grids (cylinder axis aligned with the rotor shaft) were created in the vortex path and for the rotor blades. An unstructured grid was used in the rest of the domain to keep the overall point count low; see Fig. 6. Blade pitch changes and rotation of the rotor assembly was achieved using chimera/overset grids. To allow a relative motion of the rotor to the fixed ground plane, five chimera blocks were created, one for each blade (pitch), one for the rotor assembly (rotation), one for the ground plane (ground plane inclination) and one as static background; see Figs. 6 and 7. For the simulations hole definition geometries were provided and automatic hole cutting was not used.

Compared to the teeter rotor head assembly in the experiment, a simplified rotor head was modeled in the numerical simulations. The two blades were connected by a cylindrical structure that can be regarded as a generic teeter rotor head; see Fig. 8. It was expected that the chosen strategy allows for a better prediction of the flow field close to the hub compared to not modeling the hub or placing a rotationally symmetric body between the rotor blades. The two individual blade meshes were connected by chimera interpolation and the blade surfaces overlapped in the interpolation region.

To improve chimera interpolation, care was taken that in the overlapping regions the cell sizes and orientations of the different grids matched as far as possible. For example, the interpolation regions where the tip vortex and the vortex sheet were interpolated between the blade and the

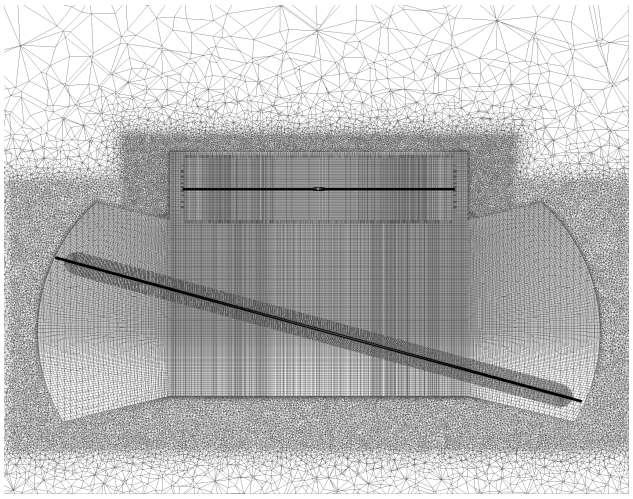

Fig. 6: Schematic showing the structured mesh in the region of interest and the unstructured mesh in the surrounding computational domain.

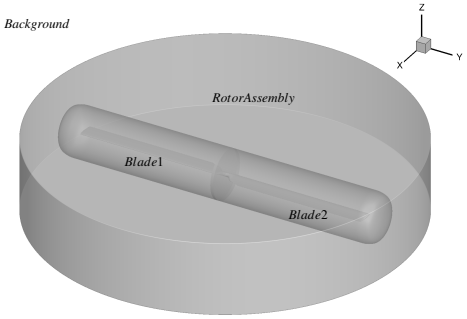

Fig. 7: Schematic showing the used chimera setup for the rotor assembly.

rotor assembly were identical; see Fig. 9. For the ground, plane this was not possible because otherwise large deformations of the background grid would have been necessary to allow for different ground plane inclination angles. By keeping the cylindrical structured grid in the tip vortex path undistorted, grid influences on the vortex preservation downstream to the ground plane could be prevented.

The rotor blades were meshed using an O-grid in sections perpendicular to the rotor blade quarter-chord axis (see Figs. 8 and 9) and a C-type topology along the blade axis; see Figs. 7 and 8. In comparison to the blades used in the experiments, the tip as well was the trailing edge tab were rounded, but the projected surface area of the blade and the chord length was kept constant. 240 cells were used in wraparound direction, 70 in normal direction and, 164 in radial direction.

The grid in the vortex trajectory consisted of 720 cells in peripheral direction. In the z and r direction (i.e., perpendicular to the vortex trajectory) a grid spacing of 1.75mm (3.9% chord) was used. The farfield boundary had a spherical shape and was placed at a distance of $11R$ from the rotor head. Details on the mesh dimensions are given in Table 2.

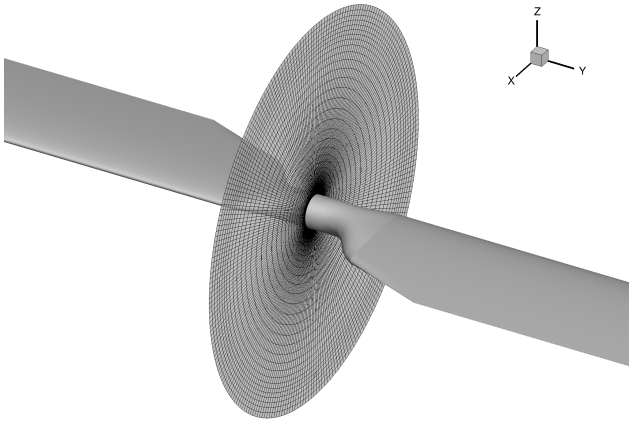

Fig. 8: Schematic showing the generic rotor hub and a slice through the grid in the blade to blade chimera interpolation region.

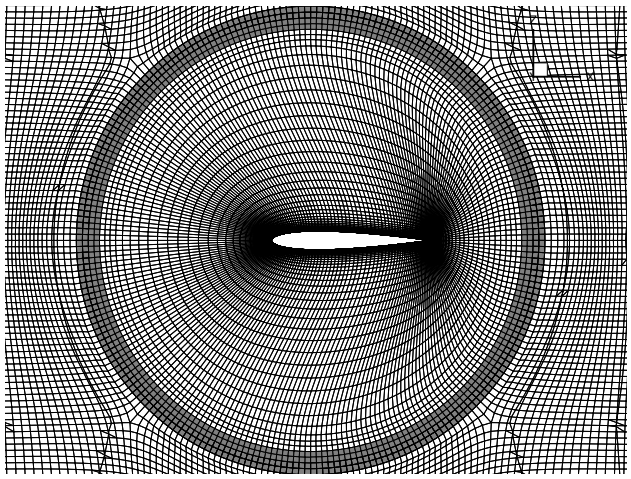

Fig. 9: Schematic showing the chimera interpolation region (grey) between the blade and rotor assembly grids.

4.3 Simulation Process and Convergence Criteria

The simulations were started with a blade pitch angle of $\Theta_0 = 6^\circ$ and a time step size of $\Delta\psi_b = 9^\circ$ (40 time steps per revolution) using 150 inner iterations. Ten rotor revolutions were computed to transport the starting vortex downstream to the ground plane, and the density residual was reduced by more than 3.5 orders of magnitude compared to the first overall density residual.

Then, the time step size was reduced to 360 time steps per revolution ($\Delta\psi_b = 1^\circ$) using 100 inner iterations to achieve convergence. Three criteria had to be fulfilled in order to consider a simulation converged. First, in a physical time step the density residual had to drop below $1 \cdot 10^{-6}$ in comparison to the overall first density residual. Second, the starting vortex had to be transported out of the region of interest. In addition, the average thrust had to be constant over multiple revolutions. Subsequently, the rotor was trimmed to the experimental thrust values. The simulation was continued until convergence was reached for the correct thrust level.

Table 2: Mesh dimensions.

	Number of points
Blade	$3.0 \cdot 10^6$ per blade
Rotor Assembly	$13.1 \cdot 10^6$
Ground Plane	$1.7 \cdot 10^6$
Background	$45.8 \cdot 10^6$
total	$66.6 \cdot 10^6$

5. RESULTS AND DISCUSSION

Two different ground plane inclination angles ($\Theta_{GP} = 0^\circ$ and $\Theta_{GP} = 15^\circ$) were investigated. To allow for a better comparison between these two test cases, the same coordinate system was used (see Figs. 1 and 4) and the terminology of the inclined ground plane was utilized for both cases. Therefore, in the subsequent sections the terms *uphill* (i.e., $r/R < 0$) and *downhill* (i.e., $r/R > 0$) were used for both cases, even though they do not have any significance for the parallel ground plane.

The objective of the current work was to assess the flow field at various levels of detail based on instantaneous, phase-averaged, and time-averaged experimental and numerical results. The unsteadiness of the rotor flow in terms of variation of vortex center positions and swirl velocity as well as the effects of inclined ground planes on the flow field and on the rotor inflow were assessed. Numerical simulations were correlated to the experimental data and the accuracy of the computed flow solutions was assessed. As only a limited number of converged rotor revolutions was available, phase-averaging of the numerical results was not done because the results did not show significant fluctuations and, therefore, the differences between phase-averaged and instantaneous numerical results were negligible.

The experiments were performed with a constant collective pitch angle of $\Theta_0 = 6^\circ$. Therefore, the thrust varied slightly for the different ground plane inclination angles as pointed out by Milluzzo et al. [19]. The thrust conditions at which the experimental data were recorded were matched by the trimmed numerical simulations with a maximum deviation of 4%; see Table 3.

Table 3: Overview of thrust coefficients in experiment and simulation.

	$\Theta_{GP} = 0^\circ$	$\Theta_{GP} = 15^\circ$
$C_{T,\text{experiment}}$	0.003877	0.003565
$C_{T,\text{simulation}}$	0.003821	0.003717

5.1 Vorticity Contours

In Figs. 10 and 11, out-of-plane vorticity contours were used to compare an instantaneous experimental flow field realization to phase-averaged experimental and numerical data for both ground plane inclination angles. The measured phase-averages were ensemble-averaged over 500 instantaneous flow field realizations recorded at the same rotor azimuth angle.

The instantaneous experimental contour for the parallel ground plane showed clearly defined vortices which persisted downstream to the ground plane; see. Fig. 10 (a). When comparing this to the phase-averaged contour in Fig. 10 (b) it could be seen that for all wake ages the phase-averaged vortices were smeared (as expected). For older wake ages (closer to the ground plane) this effect was increased and the coherent vortex with concentrated vorticity appeared progressively more diffused. This was an effect from both vortex wandering and also from increased physical diffusion of the coherent vortices for older wake ages.

When comparing the instantaneous experimental data to the numerical result it could be seen that the vortices were smeared out; compare Figs. 10 (a) and (c). The vortex core sizes were correlated better with the phase-averaged data. This was due to the used numerical approach (URANS) that inherently averages out turbulent fluctuations and small scale flow structures. However, it was found that there was still a good correlation of the computed vortex center positions to the phase-averaged experimental results. Only the rotor wake contraction was slightly over-predicted. The vortex sheets visible in the experimental data were also computed by the numerical simulations.

The same general observations made for the parallel ground plane were, with some exceptions, also true for the inclined ground plane; compare Figs. 10 and 11. One difference was observed when comparing the instantaneous to the phase-averaged data. For the inclined ground plane, the phase-averaged vortices appeared to be less blurred. This indicated that tip vortex wandering was less significant. Hence, the inclined ground plane reduced the vortex wandering. This trend was less distinct at the downhill side of the inclined ground plane. Also, the effect form the inclined ground plane on the vortex trajectory was more pronounced uphill, whereas on the downhill side the vortex trajectory was only little affected. These qualitative statements are quantified in the following sections.

The correlation between the phase-averaged data and numerical results showed greater differences for the inclined ground plane, when compared to the parallel ground plane. The rotor wake contraction was over-predicted with larger discrepancies at the downhill side. However, it should be noted that only one flow field realization was shown here for the CFD and that averaging over a greater amount of numerical results (significantly more rotor revolutions) might alter (improve/degrade) the correlation. Nevertheless, the stabilizing effect of the inclined ground plane was visible in the numerical simulations and the measurements, i.e., the vortex structures were more coherent and the vorticity levels were higher compared to the parallel ground plane at comparable thrust levels in the simulation (given in Table 3); compare Figs. 12 (c) and 13 (c).

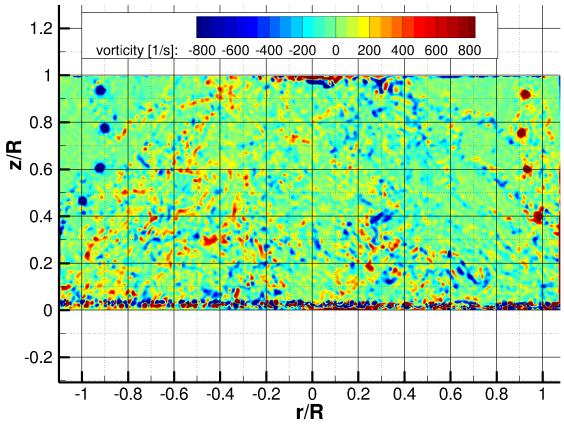

(a) Measured instantaneous flow field realization.

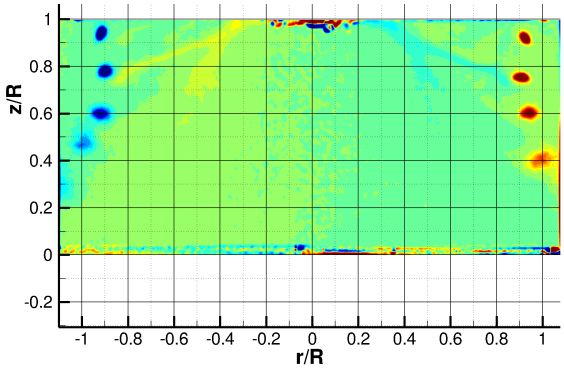

(b) Phase-averaged measured data.

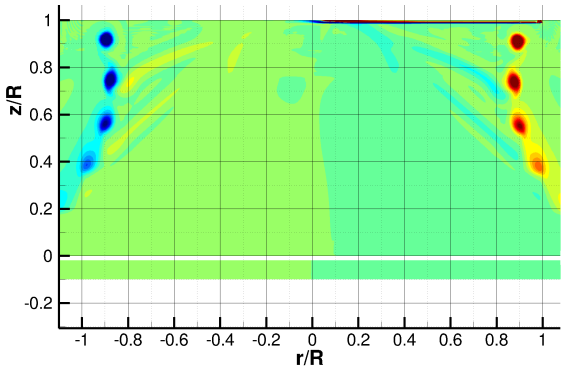

(c) CFD.

Fig. 10: Comparison of out-of-plane vorticity at a ground plane inclination of $\Theta_{GP} = 0^\circ$ at $\psi_b = 0^\circ$ of the reference blade.

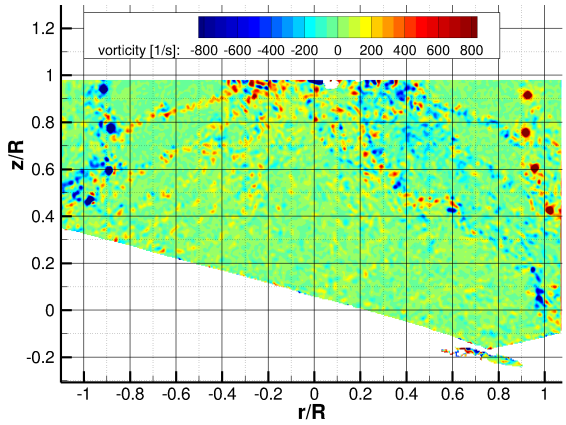

(a) Measured instantaneous flow field realization.

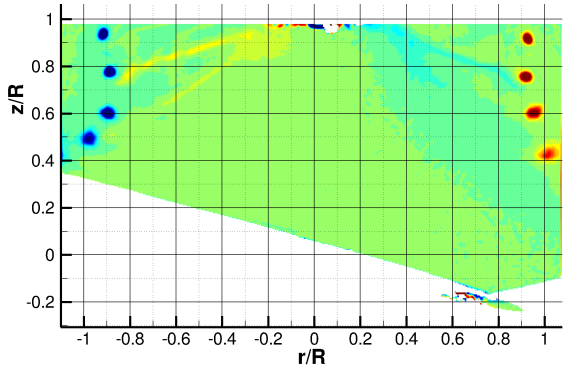

(b) Phase-averaged measured data.

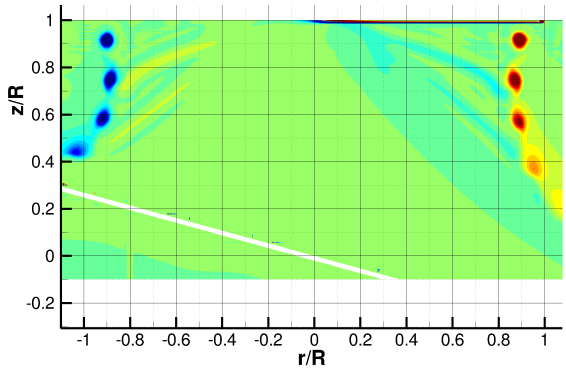

(c) CFD.

Fig. 11: Comparison of out-of-plane vorticity at a ground plane inclination of $\Theta_{GP} = 15^\circ$ at $\psi_b = 0^\circ$ of the reference blade.

5.2 Vortex Center Positions and Vortex Wandering

To quantify the qualitative findings from the out-of-plane vorticity contours discussed before, a detailed evaluation of the vortex centers and their convection was made. A comparison between the vortex center positions of the instantaneous flow field realizations with the phase-averaged and numerically predicted locations was made. A description of the automated vortex center detection algorithm is given next, followed by the evaluation of the data.

5.2.1 Vortex Center Detection In order to automatically process the experimental and numerical data sets, a vortex center identification algorithm first proposed by Michard et al. [21] and described in Graftieaux et al. [22] was adapted. In the algorithm, a dimensionless scalar function Γ_1 is defined at a point P in the flow field. As the PIV data were sampled at discrete spatial locations and the numerical results were interpolated to a Cartesian grid, an approximate version of the function was used [22]. The algorithm equates Γ_1 for a fixed point P in a two-dimensional dataset to:

$$\Gamma_1(P) = \frac{1}{N}\sum_S \frac{(\mathbf{P}\wedge\mathbf{U})\cdot\mathbf{z}}{\|\mathbf{P}\|\cdot\|\mathbf{U}\|} = \frac{1}{N}\sum_S \sin(\Theta_M)$$

S is a two-dimensional area surrounding P, M lies in S, and $\mathbf{z}$ is the unit vector normal to the measurement plane. Θ_M represents the angle between the velocity vector $\mathbf{U}$ and the radius vector $\mathbf{P}$ [22]. N depicts the number of points in S. In the current study, only the points directly surrounding P were used to evaluate Γ_1. If the vortex is axisymmetric, the center is located where $\Gamma_1 = 1$. Hence, for the current application, a lower bound had to be defined to account for the asymmetry of the swirl velocity profile due to the rotor downwash velocity. In [22] a threshold value of $\Gamma_1 \geq 0.9$ was suggested for a different application.

Furthermore, as only the tip vortices were of interest in the present study, a minimum threshold for the vorticity was defined to exclude any small-scale vortical structures. The minimum was defined as a fraction of the vorticity of the youngest vortex of interest ($\zeta = 180^\circ$), because it contained the highest levels of vorticity in the flow field.

Depending on the processed data sets, different threshold levels were used. In addition, at older wake ages some PIV data sets showed vortex pairing, which prevented an automatic detection of the vortices. Moreover, vortex break-up resulted in ambiguous vortex centers. Such data were manually excluded form further processing. Overall, this method to detect the centers of the tip vortices proved to be simple, fast, relatively robust, and easy to implement.

5.2.2 Vortex Center Positions and Vortex Wandering The evaluation of the vortex center locations was based on 500 PIV flow field realizations per ground plane inclination angle, and wake ages of up to $\zeta = 900^\circ$ are displayed. If ambiguous vortex ages were detected, the specific flow field realization was not displayed as instantaneous result. Furthermore, due to vortex wandering (vortex position possibly outside PIV ROI) and vortex dissipation or vortex break-up the number of detected vortices for older wake ages was reduced. As the laser sheet was aligned with the trailing edge of the downhill blade, the wake ages of the tip vortices at the uphill blade are only approximate values. Moreover, on the downhill side, the vortices just passed below the rotor blade (downwash due to bound circulation), whereas on the uphill side the vortices were located in front of the leading edge of the rotor blade (upwash). For the parallel ground plane, this effect of the location of the used measurement plane could explain the asymmetry between uphill and downhill vortex center locations; see Fig. 12.

For the parallel ground plane, the phase-averaged vorticity contours indicated that the amount of vortex wandering was increased for older wake ages when compared to younger wake ages; see Fig. 10. This was also observed when looking in detail at the vortex center positions; see Fig. 12. In particular, the standard deviations of the vortex center locations in radial and axial direction grew by a factor of 4 and 3 respectively from $\zeta = 180^\circ$ to $\zeta = 720^\circ$. In addition the vortex centers detected in the phase-averaged experimental data did not fully correspond to the mean of the instantaneous vortex centers. Vortex wandering, vortex pairing, and vortex break-up also influenced the detected vortex center locations in the phase-averaged data.

When comparing the numerical to the experimental results it was found that on the uphill side ($r/R < 0$) the computed vortex center positions were within or close to the ellipsoids enclosing 95.44% of the experimental instantaneous vortex center positions (two standard deviations); see Fig. 12. Therefore, the numerical vortex trajectory on the uphill side was comparable to a single flow field realization found in the experiment. On the downhill side, the correlation was weaker, and at a wake age of $\zeta = 720^\circ$ no vortex center could be found using the previously described algorithm. That is, the vortex was already significantly dissipated. On the uphill side a vortex center was found, as the wake age was slightly lower than the approximated $\zeta = 720^\circ$ (as discussed previously).

For the inclined ground plane the findings described earlier when evaluating the out-of-plane vorticity contours could be confirmed when looking at the detailed investigation of the vortex center locations; compare Figs. 11 and 13. The vortex centers in the phase-averaged data correlated better to the mean of all instantaneous vortex centers. Compared to the parallel ground plane (Fig. 12) the standard deviations were significantly lower for all wake ages on the uphill and downhill side. Hence, the finding that the inclined ground plane reduced the unsteadiness in the flow field could be substantiated. Also, the significantly lower occurrence rate of vortices older than $\zeta = 720^\circ$ for the parallel ground plane supported this. Moreover, the areas within which vortex centers were located were more circular than elongated for the inclined ground plane. That is, no preferred direction of motion of the vortex centers could be found for the inclined ground plane.

As for the parallel ground plane, a vortex center could not be detected on the downhill side for a wake age of $\zeta = 720^\circ$ for the numerical simulation; see Fig. 13. Moreover, the computed vortex trajectory on the uphill and downhill sides were further apart from the experimental values when compared to the parallel ground plane; compare Figs. 12 and 13. The rotor wake contraction was over-predicted.

5.3 Vertical Velocity Profiles through Vortex Centers

In this section, the evolution of the tip vortices was assessed based on vertical velocity profiles through the detected vortex centers. Leishman et al. used a one-bladed rotor with blades of comparable dimensions and investigated tip vortices in detail using three-component laser doppler velocimetry (LDV) [23]. To properly characterize the velocity profiles in the tip vortices, a grid spacing of 0.2 mm was used over the vortex cores [23]. In order to capture the whole flow field underneath the rotor, relatively large ROIs had to be used in the current study. This resulted in a coarser interrogation grid compared to [23].

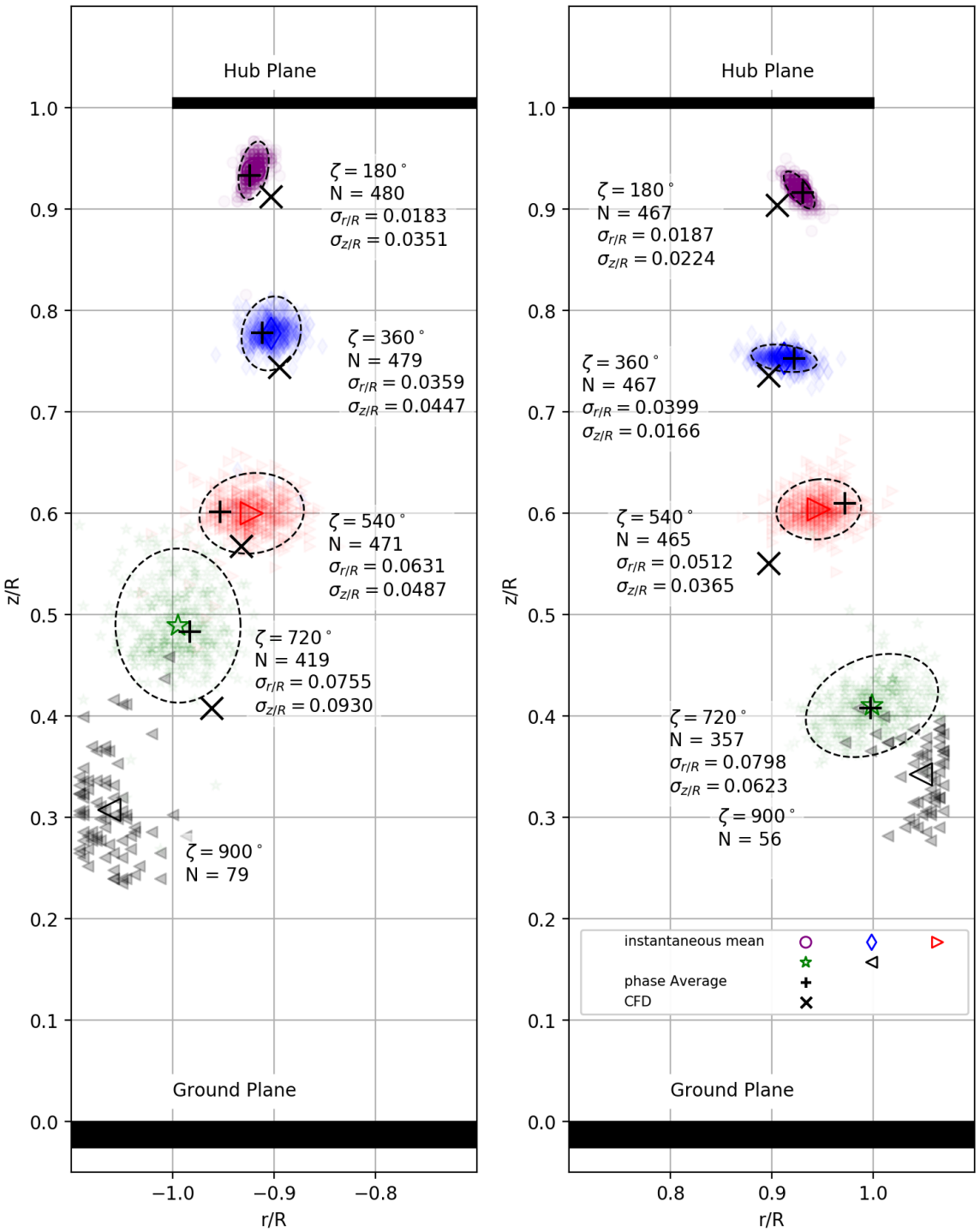

(a) uphill (b) downhill

Fig. 12: Vortex center position at $\Theta_{GP} = 0°$. Standard deviational ellipsoids (2σ) are shown for wake ages up to $\zeta = 720°$. Wake ages at the uphill side are approximate values; see Fig. 5. Identified number of vortex centers, N, is indicated for each wake age. Standard deviations $\sigma_{r/R}$ and $\sigma_{z/R}$ given in normalized coordinates (r/R, z/R).

Consequently, the subsequent comparison of vertical velocity profiles through the detected vortex centers should not be viewed as a detailed measurement or simulation of tip vortices and their properties, but shall rather show the similarities and differences between the available datasets, namely instantaneous and phase-averaged experimental results, and numerical simulations. Due to the used resolution, peak swirl velocities were probably cut off and were therefore underestimated.

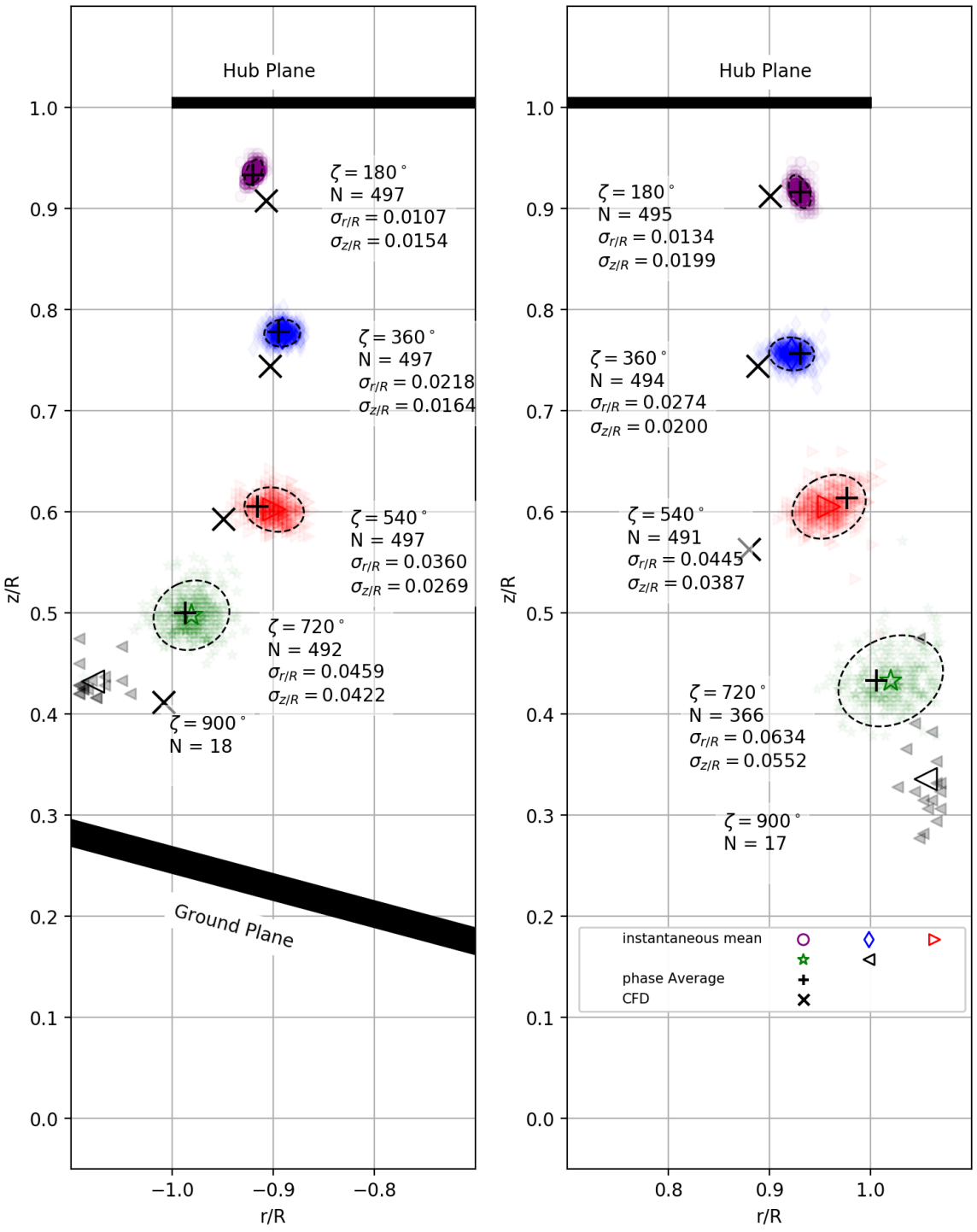

(a) uphill

(b) downhill (ground plane located below shown region)

Fig. 13: Vortex center position at $\Theta_{GP} = 15°$. Standard deviational ellipsoids (2σ) are shown for wake ages up to $\zeta = 720°$. Wake ages at the uphill side are approximate values; see Fig. 5. Identified number of vortex centers, N, is indicated for each wake age. Standard deviations $\sigma_{r/R}$ and $\sigma_{z/R}$ given in normalized coordinates (r/R, z/R).

5.3.1 Data Processing The automatically detected vortex center locations previously described were used. Velocity profiles were extracted in horizontal planes at these locations, and no further data processing was done. In particular, this means that the vortex convection velocity was not subtracted to get the isolated swirl velocity effect (and thus only the vertical velocity v_z is shown). All velocity profiles were centered at the detected vortex center location to be able to compare the profiles properly. Averaged instantaneous velocity profiles were computed by taking the

mean of the vortex-collocated instantaneous velocity profiles. As no vortex center could be detected for a wake age of $\zeta = 720^\circ$ on the downhill side in the numerical simulations, CFD velocity profiles were not shown for this wake age.

5.3.2 Results Vertical velocity profiles for wake ages up to $\zeta = 720^\circ$ for the parallel ground plane are shown in Fig. 14. When centering the measured instantaneous vertical velocity profiles, a small scatter band could be identified which closely resembled the mean. This was true up to the oldest wake age investigated. Viscous diffusion was apparent, as the peak-to-peak velocity amplitudes were reduced for older vortex ages and the gradient of the velocity profile between the peaks was decreased.

In contrast to that, the phase-averaged velocity profile deviated from the vortex-collocated averaged instantaneous profile already at a wake age of $\zeta = 180^\circ$. The peak-to-peak velocity amplitudes were lower. However, the profiles still showed the characteristic swirl velocity peaks at the edge of the vortex core. The numerical simulations followed the same trend and were in good agreement with the phase-averaged data. The good correlation between phase-averaged and numerical data was already pointed out when discussing the out-of-plane vorticity contours and the vortex center locations, and this could be confirmed here; see Figs.10 and 12. A large discrepancy between the phase-averaged and numerical velocity profile was only found at a wake age of $\zeta = 540^\circ$ on the downhill side. The velocity profiles were shifted, i.e., the vortex center locations were predicted at different locations on the velocity profile; see Fig. 14 (b). The vortex was already significantly diffused in the numerical simulation and the phase-averaged experimental result, which seemed to be a problem for the algorithm to detect the vortex center correctly. However, for a wake age of $\zeta = 720^\circ$, the numerical and phase-averaged experimental results were in excellent agreement.

The same comparison was made for the inclined ground plane; see Fig. 15. For early vortex ages $\zeta = 180^\circ$ the phase-averaged velocity profiles were in good agreement with the averaged instantaneous result. In comparison to the parallel ground plane, the correlation was significantly better. This confirmed the findings presented earlier, that fluctuations were reduced for $\Theta_{GP} = 15^\circ$ when comparing the out-of-plane vorticity contours (Figs. 10 and 11) as well as when comparing the vortex center locations (Figs. 12 and 13). Over the entire range of investigated wake ages, the correlation between the numerical simulations and the experimental data was worse compared to the parallel ground plane; compare Figs. 14 and 15. Nevertheless, the numerical simulation predicted the trends seen in the phase-averaged data well.

5.4 Time-Averaged Flow Field

Time-averaged in-plane velocity magnitudes were calculated for the two ground plane angles by averaging instantaneous flow field realizations at increments of $\Delta\psi_b = 10^\circ$. For time-averages of the experimental data, ten images per rotor azimuth were used. For the numerical simulation, the result was averaged over one rotor revolution. Excursions in the slipstream boundary visible in the numerical results were caused by the relatively low sample size of the numerical data; see Figs. 16 and 17.

A more extensive experimental comparison between six different ground plane inclination angles was made by Milluzzo et al. [19]. The key findings could be confirmed by the current numerical simulations which were in good agreement with the experimental results from a flow phenomenological point of view. More details on the experimental results are given in [19] and the most important insights are summarized below and compared ot the numerical simulations.

For the parallel ground plane, the flow topology was almost symmetric to the rotor shaft axis; see Fig. 16. Two large recirculation regions were visible in the interrogation plane. When inclining the ground plane, the flow topology became asymmetric. The stagnation point on the ground plane was shifted uphill. The location of the stagnation point was in good agreement between the numerical simulation and the experiment; see Fig. 17.

In either case, the slipstream boundary was well defined. For the inclined ground plane, the downhill slipstream boundary was lifted significantly further off the ground compared to the parallel ground plane. As a consequence, a ground plane-parallel flow formed, which was strongly biased toward the downhill side. Differences in the slipstream boundary were more pronounced on the uphill side when comparing the parallel to the inclined ground plane. As discussed previously, the wake contraction was over-predicted in the numerical simulations. This could also be seen in the time-averaged flow field contours; see Fig. 16 and 17. In general, the comparisons from the time-averaged flow fields agreed well with the previously described aspects of the flow and further underpinned the findings.

Close to the rotor hub ($r/R = 0, z/R = 1$) the experimental data showed higher velocities compared to the numerical simulation for both ground plane inclinations. Hence, the chosen rotor head modeling strategy (Fig. 8) along with the numerical settings (discussed in Section 4) did not model the unsteadiness of the flow field here. A more detailed model of the rotor head would potentially improve the numerical results.

5.5 Axial Velocity Distributions

To get better insight into the inflow velocities in the rotor plane, the instantaneous, phase-averaged, and time-averaged experimental axial velocity distributions were compared to the numerical data. The objective was to assess the temporal variations of the axial velocity near the

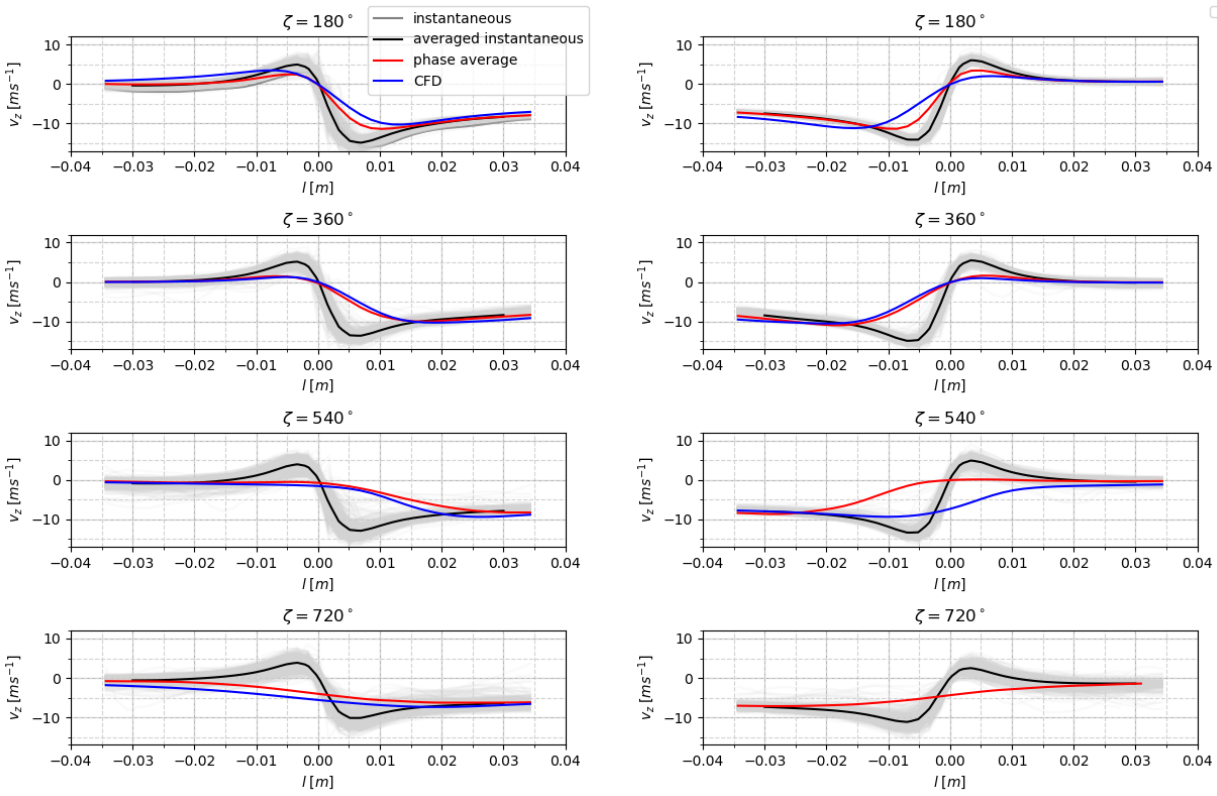

(a) uphill (b) downhill

Fig. 14: Comparison of vertical velocity (v_z) profiles in ground effect at $\Theta_{GP} = 0°$ for different wake ages. v_z was extracted in horizontal planes through identified vortex center positions.

rotor plane, as well as the dependency of axial velocity on the ground plane inclination angle.

In Fig. 18 the instantaneous axial velocity distributions are shown for $z/R = 0.98$, $\psi_b = 0°$, normalized by the theoretical hover induced velocity, and are compared to the numerical results. For both ground plane inclination angles, the largest velocity fluctuations were located close to the rotor hub and unsteadiness was reduced closer to the blade tip. This could also be seen when looking at the time-averaged contours of in-plane velocity; see Figs. 16 and 17. As the vortex center location plays a significant role for instantaneous and phase-averaged data, large differences could be seen in the axial velocity distributions between the uphill and downhill side; see also Figs. 12 and 13. On the downhill side, the tip vortex at a wake age of $\zeta = 0°$ played the predominant role (data were extracted in a plane aligned with the trailing edge of the blade; see Fig. 5). As the data were normalized by the hover induced velocity and the thrust values for the two ground plane angles were similar, i.e., the tip vortex strength was of comparable magnitude, the differences in the normalized axial velocity were small. Similar trends could be seen on the uphill side. Here, significant differences in the axial velocity were seen at the inboard sections of the blade.

On the downhill side, the computed inflow distribution was in good agreement with the experimental results. Only at the inboard section larger differences between the phase-averaged data and the numerical simulation could be found, which were caused by insufficient modeling of the unsteady flow field close to the hub (most likely caused by geometric simplifications of the hub in the numerical simulation). In contrast to that, on the uphill side, the numerical simulation showed large deviations in the inflow distribution when compared to the experimental data; see Fig. 18. Here, the most influential vortex (because closest to the rotor) was at an approximate wake age of $\zeta = 180°$, as the data were extracted in front of the blade. As the swirl velocity was under-predicted on the uphill side (see Figs. 14 and 15) and the vortex position was not computed correctly (see Figs. 12 and 13) this also heavily influenced the instantaneous inflow distribution.

Similar trends observed in the phase average for the axial velocity distributions at a blade azimuth angle of $\psi_b = 0°$ were also found in the time-averaged velocity distribution; see Fig. 19. The experimental data indicated that the inflow was only significantly influenced at inboard sections of the blade on the uphill side. For the time average, the numerical results correlated better with the experiment. The differences on the uphill side were reduced compared to the results obtained at $\psi_b = 0°$ (phase-averaged data), even though the overall correlation was still poor closer to the rotor hub. On the downhill side the over-predicted

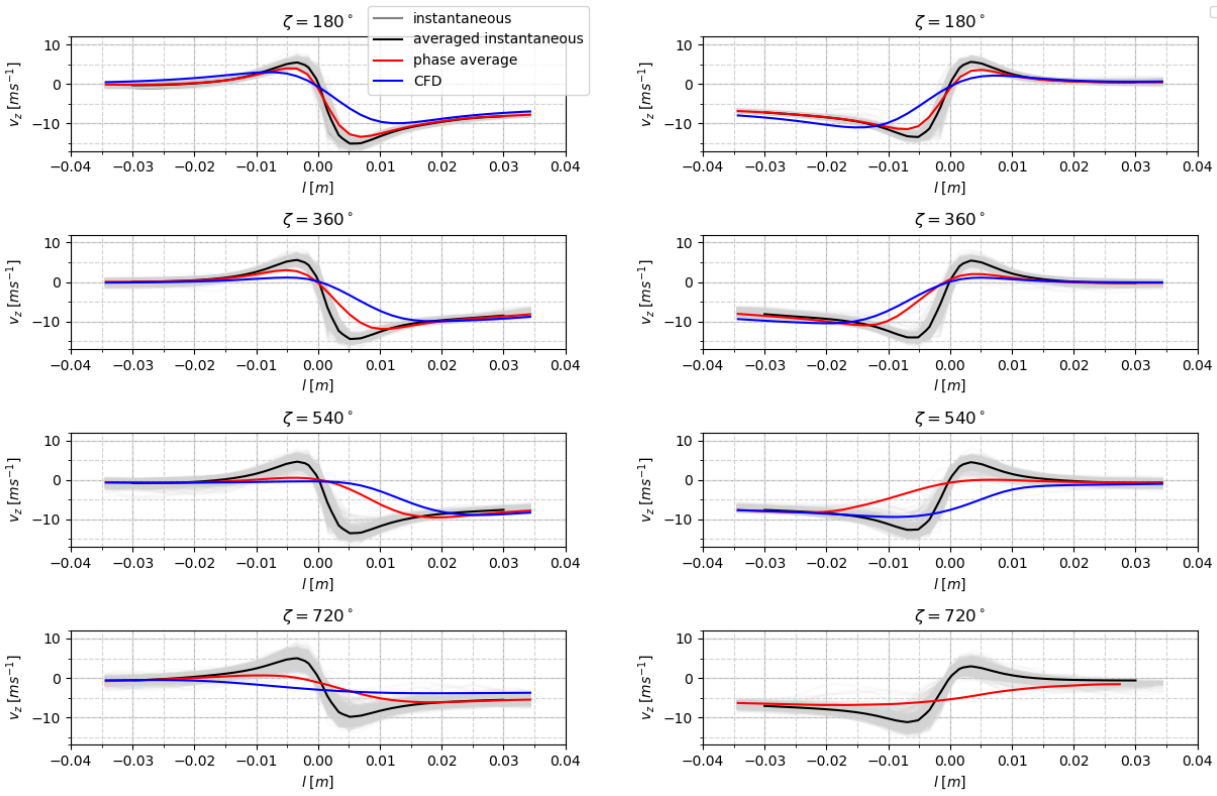

(a) uphill (b) downhill

Fig. 15: Comparison of vertical velocity (v_z) profiles in ground effect at $\Theta_{GP} = 15°$ for different wake ages. v_z was extracted in horizontal planes through identified vortex center positions.

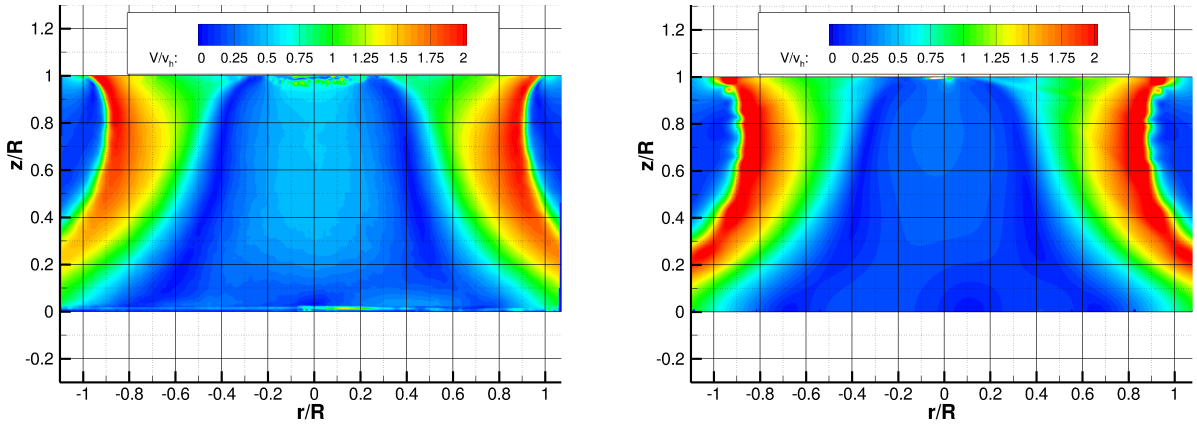

(a) Experiment. (b) CFD.

Fig. 16: Time-averaged contour of in-plane velocity magnitude normalized by the theoretical hover induced velocity for the rotor operating in parallel ground effect. Experimental results recorded in increments of $\Delta\psi_b = 10°$ over multiple revolutions (10 images per azimuth). Numerical results averaged over one rotor revolution in increments of $\Delta\psi_b = 10°$ (i.e., 36 slices).

wake contraction previously described could also be seen; see Fig 19. The peak amplitude matched the experimental data well.

6. CONCLUDING REMARKS

This paper compared the effects of a parallel ground plane to the effects of a ground plane at an inclination angle of $\Theta_{GP} = 15°$ on the flow field of a hovering two-bladed 0.8 m-diameter rotor. Flow field measurements using par-

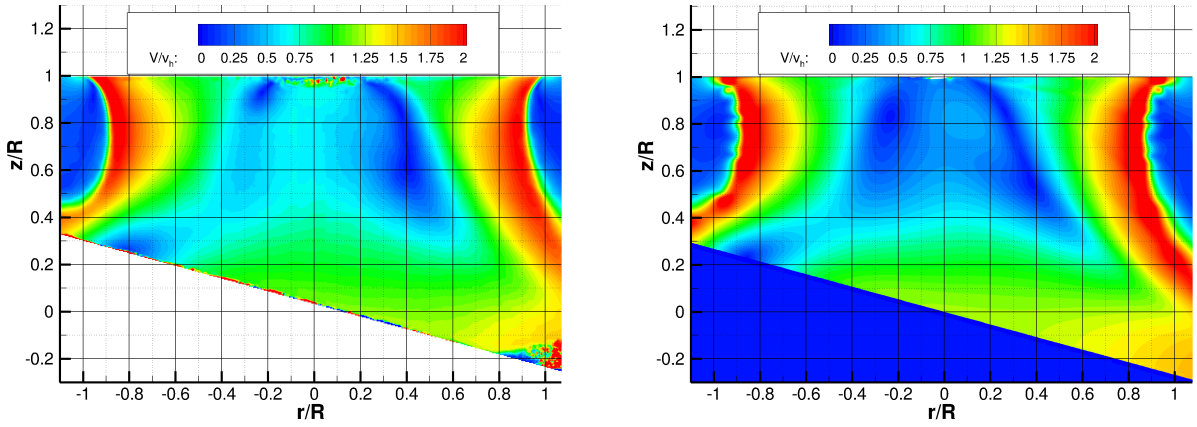

(a) Experiment. (b) CFD.

Fig. 17: Time-averaged contour of in-plane velocity magnitude normalized by the theoretical hover induced velocity for the rotor operating in non-parallel ground effect ($\Theta_{GP} = 15°$). Experimental results recorded in increments of $\Delta\psi_b = 10°$ over multiple revolutions (10 images per azimuth). Numerical results averaged over one rotor revolution in increments of $\Delta\psi_b = 10°$ (i.e., 36 slices)

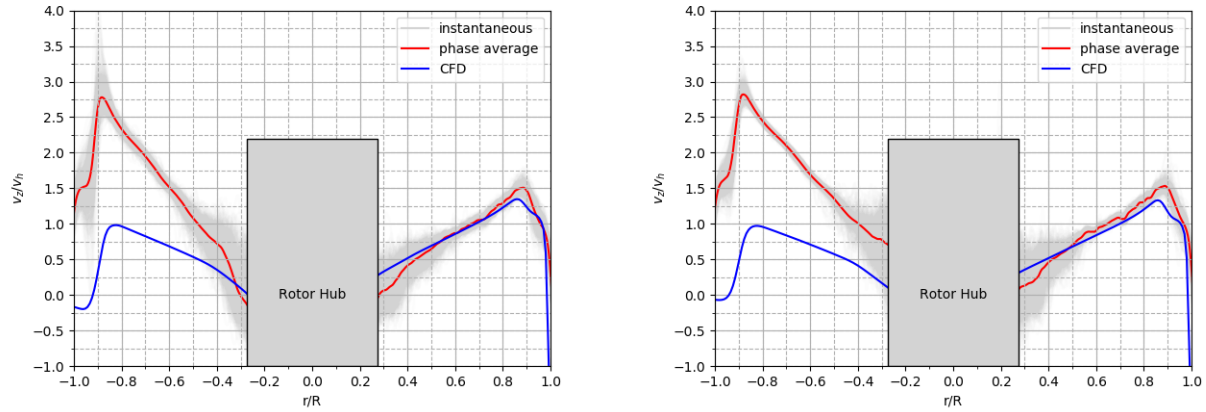

(a) $\Theta_{GP} = 0°$ (b) $\Theta_{GP} = 15°$

Fig. 18: Comparison of instantaneous experimental, phase-averaged experimental and, computed radial distribution of axial velocity (v_z) through the rotor normalized by the theoretical hover induced velocity (v_h). Values were extracted at $z/R = 0.98$ and $\psi_b = 0°$.

ticle image velocimetry and numerical simulations using the unsteady Reynolds-averaged Navier–Stokes (URANS) equations were made. The flow field beneath the rotor and the inflow distribution were examined. The experiments and simulations revealed that the behavior of the vortex flow was significantly altered when inclining the ground plane. Furthermore, the ability to accurately compute the flow field was assessed by comparing instantaneous, phase-averaged, and time-averaged experimental data to numerical results.

When hovering over a parallel ground plane, the rotor wake was almost symmetric. This changed when the ground plane was inclined. The rotor flow field was no longer symmetric to the rotational axis. Particularly on the uphill side, the influence was evident, whereas on the downhill side the effects were less significant in terms of the vortex core locations and the time-averaged velocity contours.

Inclining the ground plane to $\Theta_{GP} = 15°$ reduced the wandering of the tip vortices for all wake ages. The detected vortex center locations were located closer to their mean location, i.e., the standard deviation of the vortex center positions was significantly reduced. This effect was found for both the downhill and the uphill side.

The numerical simulations showed good agreement form a flow phenomenological perspective. The flow topology was computed correctly, showing all major flow features and good vortex preservation. However, the wake contraction was over-predicted. For the parallel ground plane, the vortex trajectory was in good agreement with the experimental data. The correlation between the simulation and the experiment deteriorated for the inclined ground

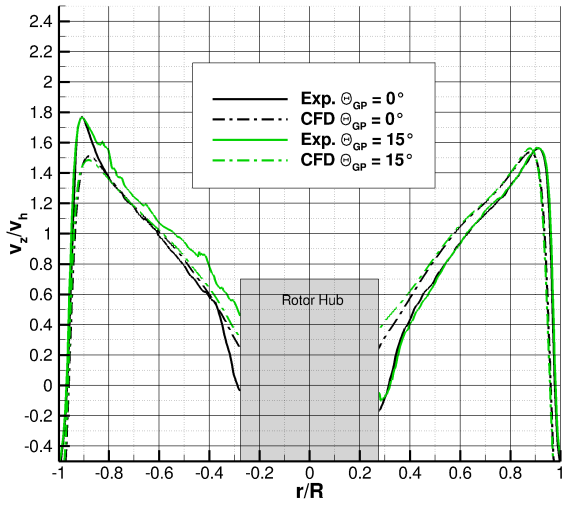

Fig. 19: Time-averaged radial distribution of axial velocity (v_z) through the rotor normalized by hover induced velocity (v_h). Values extracted at $z/R = 0.98$.

plane. It is hypothesized that because of numerical diffusion of the tip vortices the interaction with the inclined ground plane was underpredicted, and thus the asymmetry of the flow field was not fully captured.

By inclining the ground plane, the inflow was mostly affected on the uphill side and at the inboard sections, whereas on the downhill side this influence was little. On the uphill side, the numerical simulations under-predicted the magnitude of the inflow, which was more significant for the phase average compared to the time average. The numerical simulations showed good agreement with the experimental data for the downhill side for both ground plane inclination angles.

ACKNOWLEDGMENTS

The Office of Naval Research supported this work as part of the Vertical Lift Research Center of Excellence (VLRCOE) grant N0001417WX00816.

The numerical work was sponsored by the U.S. Army under grant number W911NF-17-1-0579. The views and conclusions contained herein are those of the authors only and should not be interpreted as representing those of the U.S. Army or the U.S. Government.

REFERENCES

[1]Knight, H., and Hefner, R. A., "Analysis of Ground Effect on the Lifting Airscrew," Tech. Rep. 835, NACA TN, 1941.

[2]Zbrozek, J, "Ground Effect on the Lifting Rotor," Tech. Rep. 2347, British ARC & RM, 1947.

[3]Cheeseman, I. C., and Bennett, W. E, "The Effect of the Ground on a Helicopter Rotor in Forward Flight," Tech. Rep. 3021, British ARC & RM, 1955.

[4]Fradenburgh, E. A, "The Helicopter and the Ground Effect Machine," *Journal of the American Helicopter Society*, Vol. 5, No. 4, 1960, pp. 26–28.

[5]Hayden, J. S, "The Effect of the Ground on Helicopter Hovering Power Required," *American Helicopter Society 32th Annual National V/STOL Forum Proceedings*, Montréal, Canada, May 10–12, 1976.

[6]Taylor, M. K., "Balsa-Dust Technique for Air-Flow Visualization and Its Application to Flow Through Model Helicopter Rotors in Static Thrust," Tech. Rep. 2020, NACA TN, 1950.

[7]Lee, T. E., Leishman, J. G., and Ramasamy, M., "Fluid Dynamics of Interacting Blade Tip Vortices With a Ground Plane," *Journal of the American Helicopter Society*, Vol. 55, No. 2, April 2010, pp. 1–16.

[8]Milluzzo, J., and Leishman, J. G., "Vortical Sheet Behavior in the Wake of a Rotor in Ground Effect," *AIAA Journal*, Vol. 55, No. 1, 2017, pp. 24–35.

[9]Sydney, A., Baharani, A., and Leishman, J. G., "Understanding Brownout using Near-Wall Dual-Phase Flow Measurements," *67th Annual Forum Proceedings of the American Helicopter Society*, Phoenix, AZ, May 3–5, 2011.

[10]Kocak, G., *Flow Characterization of Full, Partial, and Inclined Ground Effect*, master's thesis, Department of Mechanical Engineering, Middle East Technical Universeity, Ankara, Turkey, 2016.

[11]Newman, S. J., "The Verification of a Theoretical Helicopter Rotor Blade Sailing Method by Means of Windtunnel Testing," *The Aeronautical Journal*, Vol. 99, No. 982, February 1995, pp. 41–51.

[12]Kalra, T. S., Lakshminarayan, V. K., and Baeder, J. D., "Effect of Tip Geometry on a Hovering Rotor in Ground Effect: A Computational Study," *31st AIAA Applied Aerodynamics Conference Proceedings*, San Diego, CA, June 24–27, 2013.

[13]Kalra, T. S., *CFD Modeling and Aanalysis of Rotor Wake in Hover Interacting with a Ground Plane*, dissertation, University of Maryland, 2014.

[14]Lakshminarayan, V. K., Kalra, T. S., and Baeder, J. D., "Detailed Computational Investigation of a Hovering Microscale Rotor in Ground Effect," *AIAA Journal*, Vol. 51, No. 4, April, pp. 893–909.

[15]Govindarajan, B., and Leishman, J. G., "Predictions of Rotor and Rotor/Airframe Configurational Effects on Brownout Dust Clouds," *AIAA Journal*, Vol. 53, No. 2, 2016, pp. 545–560.

[16]Syal, M., and Leishman, J. G., "Predictions of Brownout Dust Clouds Compared to Photogrammetric Measurements," *Journal of the American Helicopter Society*, Vol. 58, No. 1, 2013, pp. 1–18.

[17]Xin, H., Prasad, J. V. R., Peters, D. A., Itoga, N., Iboshi, N., and Nagashima, T, "Ground Effect Aerodynamics of Lifting Rotors Hovering Above Inclined Ground Plane," *Proceedings of the 17th Applied Aerodynamics Conference*, Washington, D.C., June 28–July 01, 1999.

[18]Yu, K., and Peters, D.A., "Nonlinear State-Space Modeling of Dynamic Ground Effect," *Journal of the American Helicopter Society*, Vol. 50, No. 3, 2005, pp. 259–268.

[19]Milluzzo, J., Martinez, S., Drayton. S. and Davids, S., "PIV and Performance Measurements on Rotors Hovering above Inclined Surfaces," *74th Annual Forum Proceedings of the American Helicopter Society*, Phoenix, AZ, May 14–17, 2018.

[20]Schwamborn, D., Gardner, A. D., von Geyr, H., Krumbein, A., Lüdeke, H., and Stürmer, A., "Development of the DLR TAU-Code for Aerospace Applications," *International conference on aerospace science and technology*, Bangalore, India, 2008.

[21]Michard, M., Graftieaux, L., Lollini, L., and Grosjean, N., "Identification of Vortical Structures by a non-local Criterion - Application to PIV Measurements and DNS-LES Results of Turbulent Rotating Flows," *Proceedings of the 11th Conference on Turbulent Shear Flows*, Grenoble, France, 1997.

[22]Graftieaux, L., Michard, M., and Grosjean, N., "Combining PIV, POD and vortex identification algorithms for the study of unsteady turbulent flows," *Measurement Science and Technology*, Vol. 12, 2001, pp. 1422–1429.

[23]Leishman, J. G., Baker, A., and Coyne, A., "Measurements of Rotor Tip Vortices Using Three-Component Laser Doppler Velocimetry," *Journal of the American Helicopter Society*, Vol. 41, No. 4, 1996, pp. 342–353.